J. Fluid Mech. (1988), *vol.* 190, *pp.* 179–200
Printed in Great Britain

Laminar flow through slots

By E. G. TULAPURKARA†, B. H. LAKSHMANA GOWDA‡ AND N. BALACHANDRAN†

† Department of Aeronautical Engineering, Indian Institute of Technology, Madras-600036, India

‡ Department of Applied Mechanics, Indian Institute of Technology, Madras-600036, India

(Received 9 October 1986 and in revised form 6 October 1987)

Laminar flow through slots is investigated using a flow-visualization technique and the numerical solution of the Navier–Stokes equations for steady flow. In the flow situation studied here, the fluid enters an upper channel blocked at the rear end and leaves through a lower channel blocked at the front end. The two channels are interconnected by one, two and three slots. The flow-visualization technique effectively brings out the various features of the flow through slot(s). The ratio of the slot width to the channel height w/h is varied between 0.5 to 4.0 and the Reynolds number Re, based on the velocity at the entry to the channel and the height of the channel, is varied between 300 and 2000. Both w/h and Re influence the flow in general and the extent of the regions of recirculating flow in particular. The Reynolds number at which the vortex shedding begins depends on w/h. Computations are carried out using the computer code 2/E/FIX of Pun & Spalding (1977). The computed flow patterns closely resemble the observed patterns at various Reynolds numbers investigated except around the Reynolds number where the vortex shedding begins.

1. Introduction

Flow through slots is of considerable practical interest. It serves as a first step in the analysis of the flow through gas-turbine combustion-chamber walls, engine valves, slots in ejectors, in partition walls of underground tunnels, etc. Using a complex-variable technique Saddoughi (1982) developed the solution of potential flow through a slot in a horizontal channel. Tulapurkara *et al.* (1986) have extended this solution to flow through multiple slots. When the results of this potential-flow solution are compared with measurements, they find significant differences in the two flow patterns, especially beyond the slot(s). The differences are due to the fact that in the real flow situation the flow separates at the lips of the slot and regions of recirculating flow are found there. These regions cannot be predicted by potential-flow theory. To gain a better insight into the flow phenomenon, the laminar flow through slots is investigated experimentally and theoretically.

The configuration of the slot investigated in this study is shown in figure 1 (*a*, *b*). The flow enters an upper channel blocked at the rear end and leaves from a lower channel blocked at the front end. The flow can be expected to separate at points A and B (see figure 1*a*) and at some point on the side passing through the corner C_3 (figure 1*b*). The shear layers that separate at points A and B would reattach on the downstream side, giving rise to zones of recirculating flow. Now, for the flow situations where separation points are fixed, for example flow past a sharp-edged bluff body or sudden expansion, the flow phenomenon is independent of Reynolds

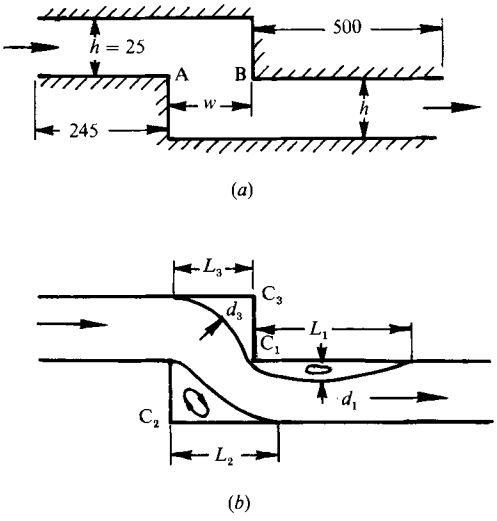

FIGURE 1. The test arrangement: (*a*) schematic arrangement of slot; (*b*) regions of recirculating flow. Dimensions in mm.

number when the latter is sufficiently high. But at low Reynolds numbers the separation, downstream reattachment and the structure of the recirculation region do depend on Reynolds number. Analogously, it can be expected that the separation, the extent and other details of the zones of recirculating flow formed aft of points A and B, would depend on the Reynolds number when it is low. Another variable which could influence the flow conditions considerably is the relative slot width w/h. It would be very interesting to see the influence of these two parameters, viz. Re and w/h, on the flow field through the slots. With a multiple slot configuration (which could be obtained by introducing plates in the width w), the flow field would be further complicated. Probably the most interesting aspect of this kind of flow is the way in which the approach flow would divide through these slots, and the consequent influence on separation and the extent of recirculating flow regions. The aim of the present investigation is to look at some of these in a systematic way when the flow is laminar.

Laminar flow occurs only at rather low Reynolds numbers but it is difficult to carry out accurate measurements of the velocity field at these low Reynolds numbers. Hence to study the flow situation experimentally, a flow-visualization study has been carried out in a water channel at various Reynolds numbers and slot widths. A theoretical solution has been obtained by numerically solving the Navier–Stokes equations for steady flow using the computer code given by Pun & Spalding (1977) in a suitably modified form. The observed flow patterns are compared with those obtained from computation and the important features are discussed.

2. Flow-visualization study

2.1. *Experimental set-up*

The experiments are carried out in a recirculating water channel. The facility consists essentially of a tank 2.5 m × 1.5 m with a depth of 150 mm (figure 2). At one end of the tank there are two sets of aluminium disks (vanes) with suitable spacing in

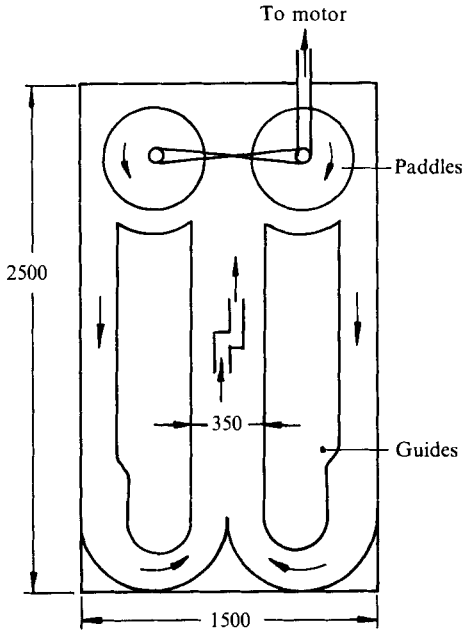

FIGURE 2. Schematic view of the flow-visualization tank. Dimensions in mm.

between. When these vanes are rotated, they act as paddles and create a flow in the tank. The flow is guided to the test section where the model is placed. The vanes are rotated by a variable speed d.c. motor which enables one to achieve a fairly wide range of flow speeds in the test section. The fluid in the tank is water and fine aluminium powder is used as tracer medium. Photographs are taken by mounting the camera at a suitable location above the model, which is lit using halogen lamps.

The flow situation used is shown in figure 1 (*a*). The channels have a height of 25 mm ($h = 25$ mm in figure 1*a*). The slot width w is varied between 12.5 to 100 mm to give the ratio w/h between 0.5 to 4. This charge in w/h is obtained by shifting the lower channel relative to the upper one. The lengths of 245 mm and 500 mm shown in figure 1 (*a*) are maintained in all cases by adding suitable lengths to the upper and/or lower channel.

The Reynolds number, based on the channel height h and the velocity in the entry region of the upper channel, is varied between 300 and 2000 by controlling the velocity in the entry region. The velocity is obtained by measuring the time taken by a marker particle to travel a specified distance.

When the flow passes through a slot, the flow field can be characterized by the separation and reattachment zones as shown in figure 1 (*b*). The extents of these regions are given by the lengths L_1, L_2 and L_3 (figure 1*b*). The Reynolds number and relative slot width w/h are varied systematically and these lengths are determined from the photographs. Multiple shots are taken when the reattachment point(s) is found to change with time and an average value of the attachment distance is calculated. The camera speed in most of the cases is $\frac{1}{8}$ s. In some cases a speed of $\frac{1}{4}$ s is also used and in all such cases the speed is indicated in the figures.

2.2. *Results and discussion*

2.2.1. *Single-slot case*

A large number of photographs were taken to systematically study the influences of Reynolds number Re and relative slot width w/h on the flow pattern. Representative photographs are presented in figures 3–5. The variations of lengths L_1, L_2 and L_3 with Re and w/h are presented in figures 6 and 7. These values of L_1, L_2 and L_3 are obtained from photographs. In all cases L_1 and L_2 could be measured without much ambiguity, but in many cases it was difficult to obtain L_3 accurately. Hence L_1 and L_2 are plotted for all cases studied but L_3 is plotted only when it could be measured with reasonable confidence. These and other features of the flow patterns are discussed below.

Influence of Reynolds number. The set of photographs in figure 3 show the influence of Reynolds number at constant value of w/h ($=1$). At low Reynolds numbers, below about 400, the flow is steady everywhere including the regions of recirculating flow (figure 3*a*, *b*). At $Re = 300$ (figure 3*a*) the recirculating region near corner C_1 (see figure 1*b* for locations of corners C_1, C_2 and C_3) has a depth (d_1 in figure 1*b*) of about $0.35h$ and length of about $1.4h$. The recirculating region near corner C_2 has a length almost equal to h. The extent of the recirculating region near corner C_3 is not clear at this Reynolds number. As the Reynolds number increases from 300 to 400 the recirculating region near corner C_1 increases in depth and in length (figure 3*b*). As seen in the photograph the large recirculating region near corner C_1 reduces the effective area of the channel in that region and the flow undergoes a significant turn. With further increase in Re the separation bubble near the corner C_1 does not remain stable and vortex shedding begins (figure 3*c*, *d*; $Re = 600$ and 800) – the fluid particles comprising the recirculating region do not remain there; they come out of the recirculating region and join the main stream. New fluid particles take their place, but they also leave after some time and this goes on with regular periodicity. After the vortex shedding begins, the depth of the separated region near corner C_1 decreases. With further increase in Re, the vortex shedding also starts near corner C_2 (figure 3*e*, $Re = 1330$). At still higher Reynolds number vortex shedding starts even near corner C_3 (figure 3*f*, $Re = 2000$). After the vortex shedding has begun, the depth of the bubble near corner C_1 does not change much with Re but the length L_1 increase gradually (see also figure 6*a*). The shed vortices are dissipated as they travel downstream, but the process becomes faster as Re increases and sometimes one sees two or three vortices in the separated regions, particularly near corner C_1 (figure 3*f*).

Figure 4 shows the influence of Reynolds number on the flow pattern when w/h is 0.5. At Re around 175 the vortex shedding was found to be practically absent (figure 4*a*). The vortex shedding starts at corner C_1 as Re increases (figure 4*b*). It can be seen that the depth of the recirculating flow region near corner C_1 is larger than that in the case with $w/h = 1$, but the depth does not change much with Re. The length L_1 increases gradually (figure 6*b*).

The influence of the Reynolds number on the flow pattern for a relatively high value of w/h, viz. 3.5, is shown in figure 5. At low Reynolds numbers, below about 800, the recirculating-flow region near the corner C_1 is absent. The vortex shedding begins near corner C_3 around $Re = 1000$ (figure 5*d*). At higher Re the vortex shedding is seen also at corner C_2 and then at corner C_1. In this case the recirculating-flow region near corner C_3 is clearly seen at various Re. It is interesting to note from the photographs in figure 5 that the depth of the recirculating region near corner C_3

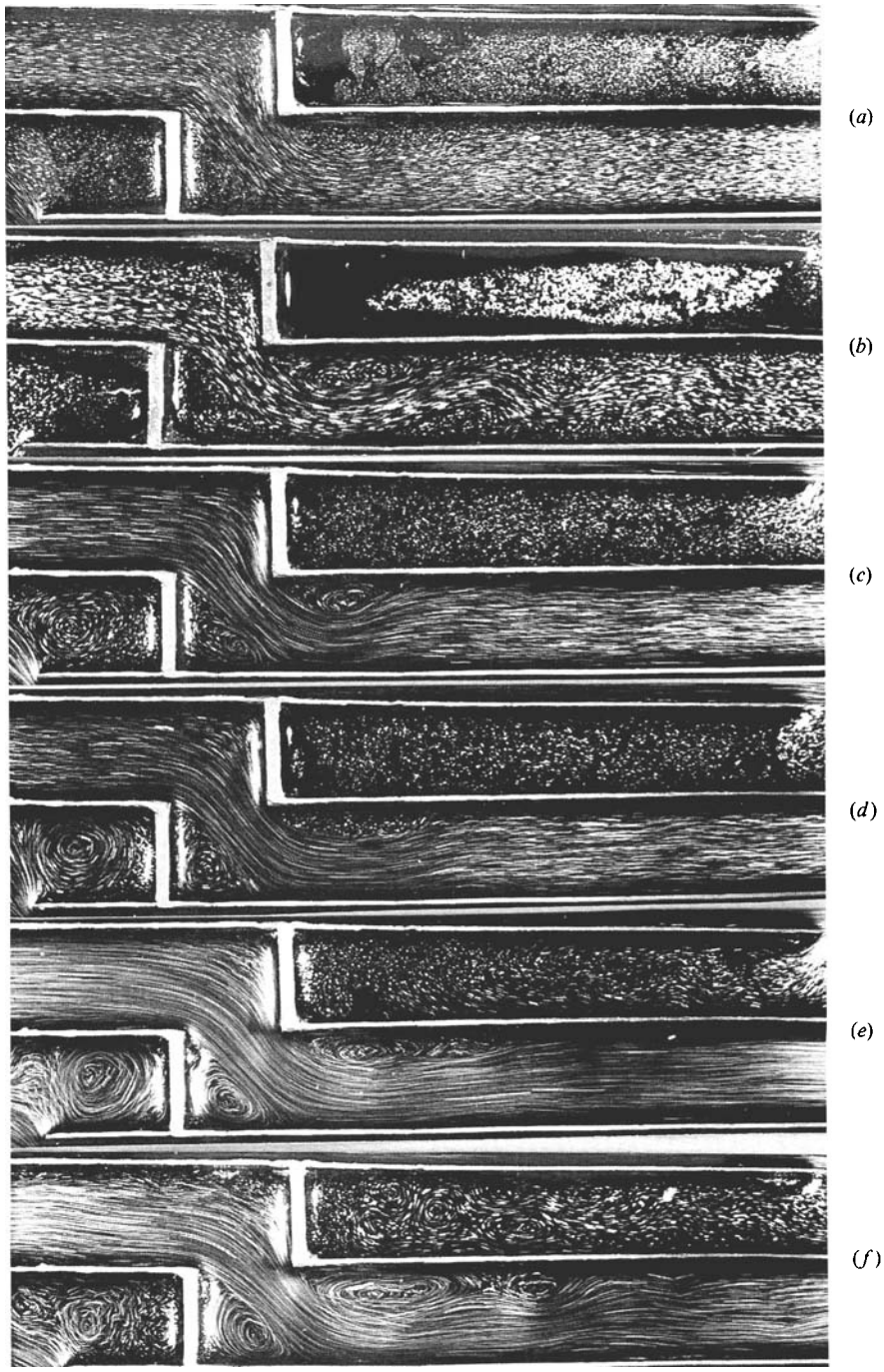

FIGURE 3. Influence of Reynolds number on flow pattern ($w/h = 1.0$). (*a*) $Re = 300$, (*b*) 400, (*c*) 600, (*d*) 800, (*e*) 1330, (*f*) 2000.

FIGURE 4. Influence of Reynolds number on flow pattern ($w/h = 0.5$). (*a*) $Re = 175$, (*b*) 300, (*c*) 400, (*d*) 600, (*e*) 1500, (*f*) 2000. Camera speed is $\frac{1}{4}$ s for (*c*), (*d*) and (*e*).

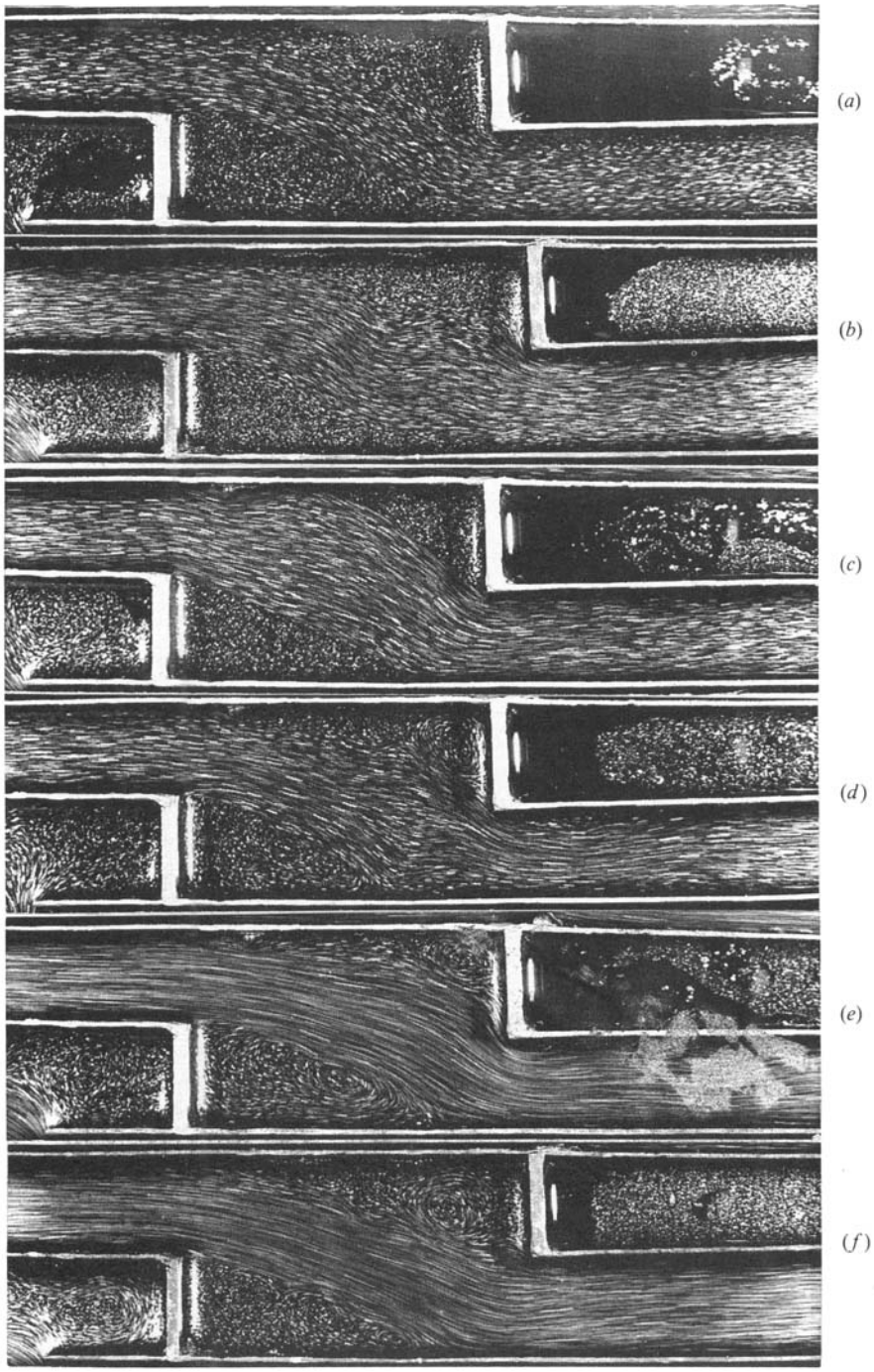

FIGURE 5. Influence of Reynolds number on flow pattern ($w/h = 3.5$). (*a*) $Re = 300$, (*b*) 600, (*c*) 800, (*d*) 1000, (*e*) 1500, (*f*) 2000.

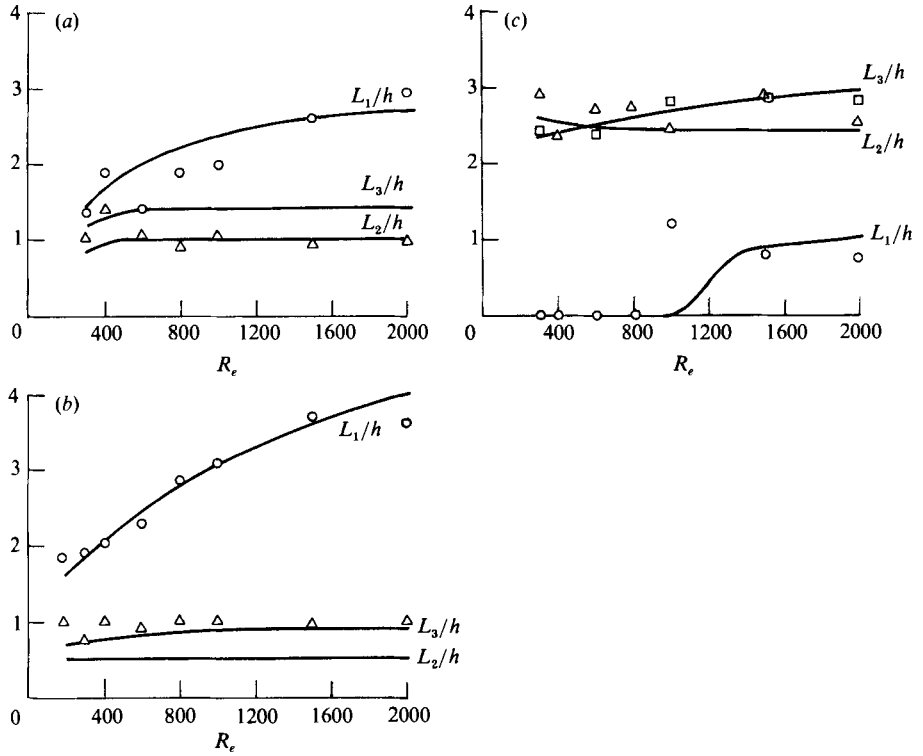

FIGURE 6. Influence of Reynolds number on L_1, L_2 and L_3. (*a*) $w/h = 1.0$, (*b*) 0.5, (*c*) 3.5. Solid lines indicate computed values. Symbols denote values from photographs: ○, L_1/h; △, L_2/h; □, L_3/h.

(depth d_3 in figure 1*b*), increases up to Re of about 800. As the vortex shedding begins near corner C_3, the depth d_3 decreases and then attains an almost constant value at higher Reynolds numbers. Figure 6(*c*) shows the variation of L_3, along with that of L_1 and L_2, with Re.

Influence of relative slot width w/h. The influence of relative slot width w/h at Reynolds numbers of 300, 600 and 2000 was investigated: results were obtained at $w/h = 0.5$, 1.0, 2.0, 3.0, 3.5 and 4.0. Some of the photographs given in figures 3–5 bring out this influence.

At the lower Reynolds number of 300, the flow is steady and there is no vortex shedding except for $w/h = 0.5$ (figure 4*b*). As the relative slot width increases the region of recirculating flow near corner C_1 decreases in length and depth and practically vanishes for $w/h = 3.0$ (similar to that in figure 5*a*).

The variations of lengths L_1, L_2 and L_3 with w/h are shown in figure 7 for $Re =$ 300, 600 and 2000. It is seen that at $Re = 300$ and 600, L_1 decreses with increase of w/h and practically vanishes for $w/h = 3$. However, for $Re = 2000$, L_1 appears to attain a constant value. L_2 and L_3 are found to increase with w/h.

It may be added that too much significance should not be attached to the lengths L_1, L_2 and L_3, but they do serve as means of comparing, quantitatively, the results of flow visualization with the numerical computations described in §3.

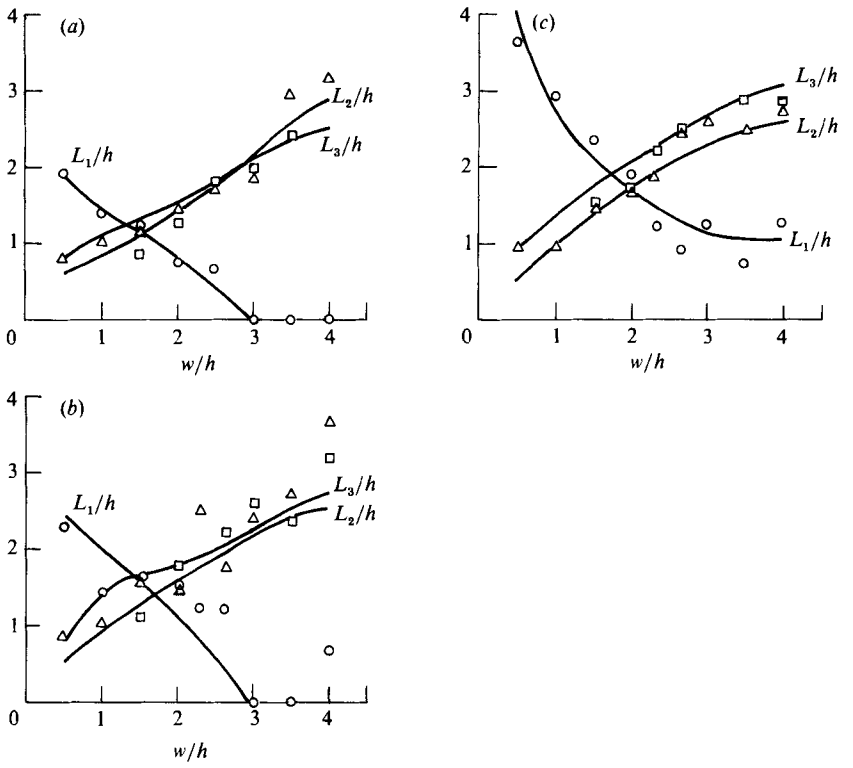

FIGURE 7. Influence of w/h on L_1, L_2 and L_3. (*a*) $Re = 300$, (*b*) 600, (*c*) 2000. Solid lines indicate computed values. Symbols denote values from photographs: ○, L_1/h; △, L_2/h; □, L_3/h.

2.2.2. *Two-slot case*

In practical applications slots can occur in a row. Hence configurations with two and three slots have also been studied. Figure 8 shows the flow patterns for the two-slot case. The widths of the two slots and the length of the plate separating the two slots are all equal to the height of the channel, 25 mm. Reynolds number varies between 250 and 2000.

In the two-slot case an additional recirculating flow region, below the plate separating the two slots, is seen. At the lowest Reynolds number, viz. 250, the flow is steady everywhere (figure 8*a*). At $Re = 400$ the vortex shedding is seen to begin near the downstream end of the plate separating the two slots. At higher Re the vortices are shed from all corners; they interact with each other and a seemingly complicated flow pattern results (figure 8*d–f*).

In the two-slot case the total slot width is $3h$. Comparing this case and the single-slot case with $w/h = 3.0$, one finds that when a plate is inserted in a slot, the regions of recirculating flow change in size. Thus if a certain configuration of the zones of recirculating flow is desired, then a suitable length and position of the plate can help in achieving it.

2.2.3. *Three-slot case*

The flow patterns for three equally spaced slots of equal width are shown in figure 9. The Reynolds number varies from 270 to 2000. There was practically no vortex shedding at Re around 270 (figure 9*a*). At Re around 400, the vortex shedding

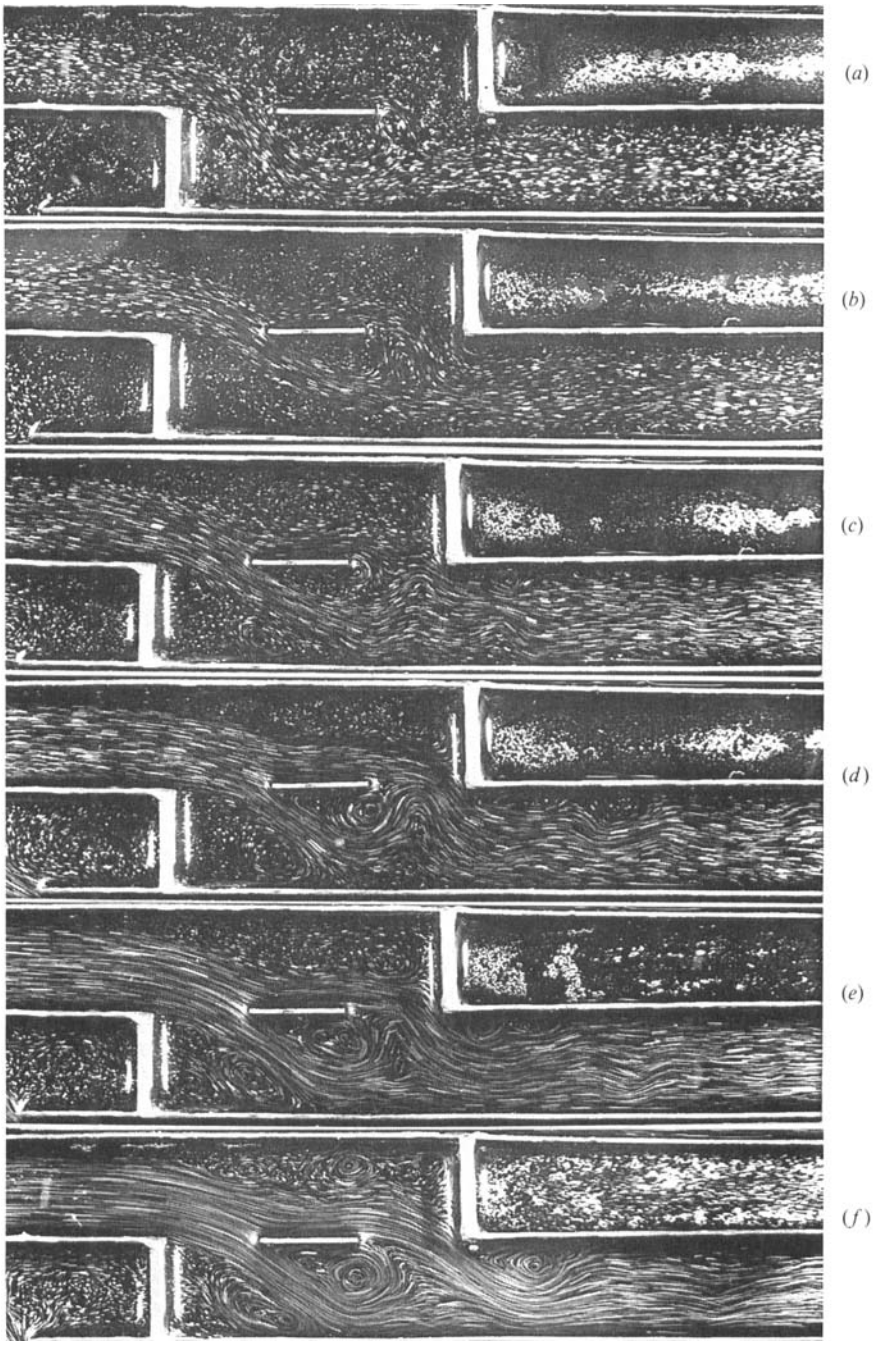

FIGURE 8. Influence of Reynolds number on flow pattern – two-slot case. (*a*) $Re = 250$, (*b*) 400, (*c*) 600, (*d*) 800, (*e*) 1330, (*f*) 2000.

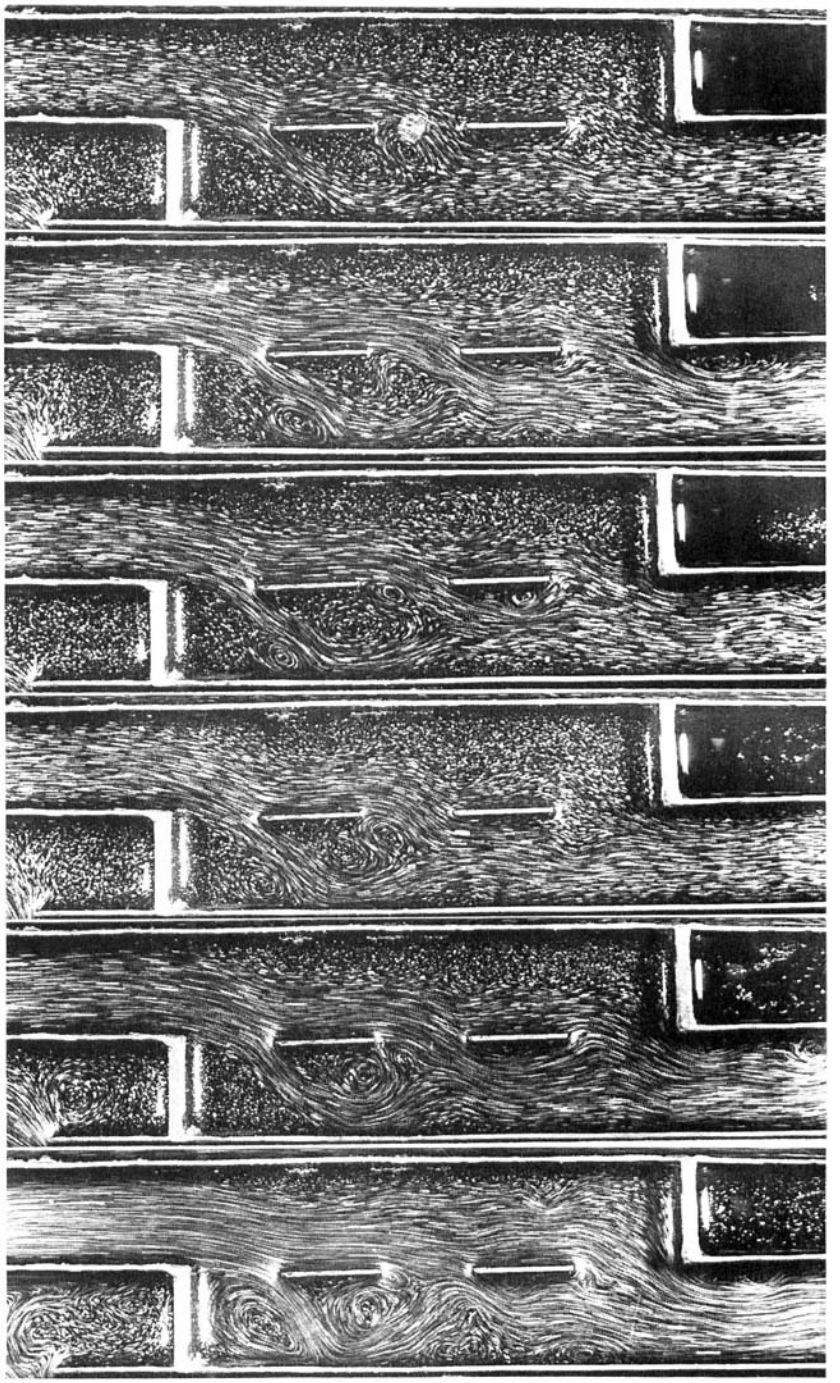

FIGURE 9. Influence of Reynolds number on flow pattern – three-slot case. (*a*) $Re = 270$, (*b*) 400, (*c*) 600, (*d*) 800, (*e*) 1330, (*f*) 2000.

appears to take place near the end of the plate separating the first and the second slot and the corner near it (figure 9*b*). At higher Reynolds numbers the formation, growth and shedding of vortices in this region becomes more frequent and pronounced. Surprisingly this kind of intense vortex formation and shedding is not noticeable in other regions of the flow field.

When the single-slot ($w/h = 1$), two-slot and three-slot cases are compared at any particular Re, it is found that the recirculating-flow region near the corner C_1 decreases (e.g. figures 3*d*, 8*d* and 9*d* or figures 3*f*, 8*f* and 9*f*). So is the case with vortex shedding at this corner. This is possibly due to two features seen in the photographs: (i) the flow velocity near the corner decreases as the number of slots increases, and (ii) the angle through which the flow turns at the corner also decreses with increase in the number of slots.

3. Computation of flow through slots

The flow-visualization study clearly shows the presence of regions of recirculating flow in the flow field. To compute such a flow field the full Navier–Stokes equations should be solved. Pun & Spalding (1977) have developed a computer code 2/E/FIX and have successfully computed flow through a pipe, sudden enlargement, etc. The name 2/E/FIX denotes a scheme for solving two-dimensional elliptic flow with a fixed grid. This code has been modified to compute flow through slots. In the subsections that follow, the basic equations and the solution procedure are briefly discussed first; then the problem-dependent features like boundary conditions, grid etc. are given. These are followed by discussion of the computed results.

3.1. *Basic equations and solution procedure*

The governing equations for a steady, two-dimensional, incompressible flow in Cartesian coordinates with standard notations are

$$\frac{\partial U}{\partial X}+\frac{\partial V}{\partial Y}=0, \tag{1}$$

$$U\frac{\partial U}{\partial X}+V\frac{\partial U}{\partial Y}=-\frac{1}{\rho}\frac{\partial p}{\partial X}+\nu\left(\frac{\partial^2 U}{\partial X^2}+\frac{\partial^2 U}{\partial Y^2}\right), \tag{2}$$

$$U\frac{\partial V}{\partial X}+V\frac{\partial V}{\partial Y}=-\frac{1}{\rho}\frac{\partial p}{\partial Y}+\nu\left(\frac{\partial^2 V}{\partial X^2}+\frac{\partial^2 V}{\partial Y^2}\right). \tag{3}$$

These equations along with boundary conditions are solved in the 2/E/FIX code by finite-difference method using staggered grid and upwind difference scheme. The computational procedure is an improved version of the algorithm SIMPLE (Semi-Implicit Method for Pressure Linked Equations). Some details of SIMPLE are given in Caretto *et al.* (1973) and a clear exposition is given in Vaselic-Melling (1977). The salient features of SIMPLE are given below so that the improvements over it in the 2/E/FIX code can be appreciated.

The equations (2) and (3) can be written in a general form as

$$\frac{\partial}{\partial X}(\rho U i)+\frac{\partial}{\partial Y}(\rho V i)-\frac{\partial}{\partial X}\left(\Gamma_i\frac{\partial i}{\partial X}\right)-\frac{\partial}{\partial Y}\left(\Gamma_i\frac{\partial i}{\partial Y}\right)=S_i. \tag{4}$$

By putting $i = U$ or V, $\Gamma_i = \rho\nu$ and $S_i = -\partial p/\partial X$ or $-\partial p/\partial Y$ in (4) we recover (2) and (3). Equation (4) can be written in a finite-difference form by integrating it over a

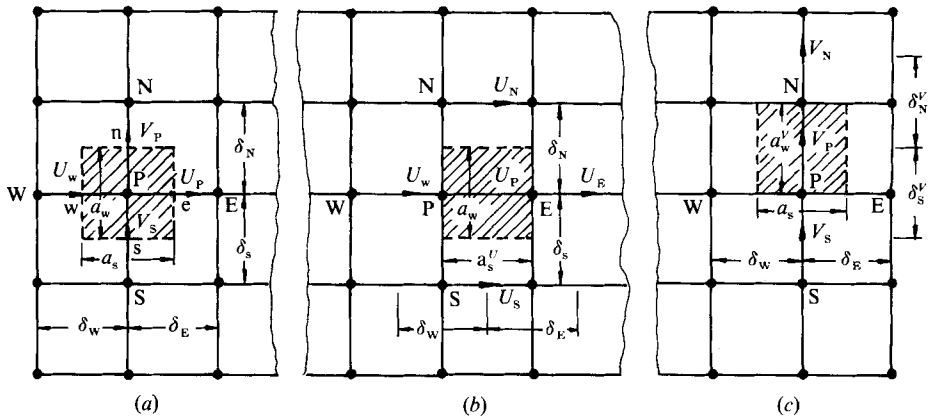

FIGURE 10. Control volumes: (*a*) for p, (*b*) for U, (*c*) for V.

finite control volume. In figure 10, the point P is a typical node and E, S, W and N are the neighbouring nodes. The points e, s, w and n lie midway between the grid nodes. In the staggered grid used in 2/E/FIX the pressure p is evaluated at grid nodes, and U and V are evaluated at points lying midway between grid nodes (figure 10*a*). The control volumes for p, U and V are indicated by dotted lines in figure 10(*a–c*).

Integrating over the control volume and using an upwind difference scheme, the finite-difference forms of (2) and (3) are

$$A_P^U U_P = \sum_{J=E,S,W,N} A_J^U U_J + a_w(p_P - p_E), \tag{5}$$

$$A_P^V V_P = \sum_{J=E,S,W,N} A_J^V V_J + a_w^V(p_P - p_E), \tag{6}$$

where $$A_P^U = \sum_{J=E,S,W,N} A_J^U, \quad A_P^V = \sum_{J=E,S,W,N} A_J^V.$$

The coefficients A_J^U and A_J^V contain convective and diffusive flow rates. a_w, a_s and a_w^V are shown in figure 10. The finite-difference form of (1) is

$$a_w(\rho U_P - \rho U_w) + a_s(\rho V_P - \rho V_S) = 0. \tag{7}$$

To obtain a solution, the sets of equations (5), (6) and (7) must be solved along with the boundary conditions. To start the solution, suitable values of U, V and p are prescribed at all nodes. A marching integration is then carried out. It involves starting at the upstream edge of the grid and proceeding line by line towards the downstream edge of the grid. The pressures appearing in (5) and (6) are not known and an iterative procedure is required. Following Patankar & Spalding (1972), guessed values of p are substituted and the finite-difference equations for U and V are set up along a vertical line. When these equations are solved using the Tri-Diagonal Matrix Algorithm (TDMA) we get approximate values denoted by U^* and V^*. Then p', the difference between the assumed and actual values of p, can be approximated as (Patankar & Spalding 1972)

$$U'_P = U_P - U_P^* = \frac{a_w}{A_P^U}(p'_P - p'_E), \quad V'_P = V_P - V_P^* = \frac{a_w^V}{A_P^V}(p'_P - p'_E). \tag{8}$$

U^* and V^* would, in general, not satisfy (7). Let M_P be the mass imbalance, i.e.

$$M_P = a_w(\rho_P U_P^* - \rho U_W^*) + a_s(\rho V_P^* - \rho V_S^*).$$

Then U', V' and p' are obtained such that M_P tends to zero or

$$a_w(\rho U_P' - \rho U_W') + a_s(\rho V_P' - \rho V_S') = -M_P. \tag{9}$$

Substituting for U_P' and V_P' from (8) in (9), gives a finite-difference equation for p_P', along the chosen vertical line. Using TDMA to solve these equations we get values of p' along the line. Then U_P' and V_P' can be obtained from (8).

The residual sources R_U and R_V are defined as the difference between the left-hand side and right-hand side of (5) and (6) respectively. If corrected values of U and V are exact, then R_U and R_V will be zero. Computations at the chosen line are repeated till values of R_U and R_V, normalized with reference quantities, are below a prescribed value. After this is achieved we proceed to the next line till entire flow field is covered. This flow field is used as a starting point for the next iteration and this process is repeated till convergence is achieved.

To hasten the convergence of the SIMPLE algorithm the values of U^* along a chosen line are corrected, in 2/E/FIX, by adding a quantity δU so that continuity across the line is satisfied. If M_i is the mass entering at the inlet to the flow domain and M_s is the mass flow across the chosen line obtained using $U_s^{*\prime}$, then $\delta U = (M_i - M_s)/(\rho a_h)$, where a_h is the height of the flow domain at the chosen grid line. To correct for any imbalance in the overall momentum, caused by the introduction of δU, the values of pressure on the line to the right of the chosen line (the flow being assumed from left to right) are changed by a uniform amount δp. It can be shown that $\delta p = -\delta U(M_i + M_s)/a_h$.

3.2. *Problem-dependent features*

In the problem being investigated here, the fluid enters the upper channel whose rear end is closed. The fluid then enters the lower channel through slot(s) and leaves at the exit of the lower channel (figure 1*a*). For the purpose of computation a rectangular domain, enclosing both the upper and lower channel, is chosen and divided into a suitable number of grid points (figure 11).

3.2.1. *Boundary conditions*

Inlet: At the inlet to the upper channel the U-component of velocity is assumed to be constant over the cross-section and V-component is taken as zero.

Outlet: U at the outlet plane need not be prescribed, but in order that the flow downstream of the exit plane does not affect the flow in the domain of calculation, $\partial U/\partial X$ is set equal to zero at exit.

Walls: The velocity components U and V are set equal to zero on the top and bottom walls of the upper and lower channels and also on vertical walls forming the slot. The middle wall is made to coincide with the nodes of the vertical velocity component. The values prescribed at the nodes lying outside the flow domain are such that they do not affect the calculations at the nodes lying inside the flow domain. The values of U and V are set equal to zero at nodes lying outside the flow domain. This way the mass flow rate through the duct is not affected.

To start the computations the values of the flow variables must be prescribed at all nodes, using guessed values. As initial distributions, U equal to its value at the inlet and V and p equal to zero are prescribed at all nodes except those lying in the

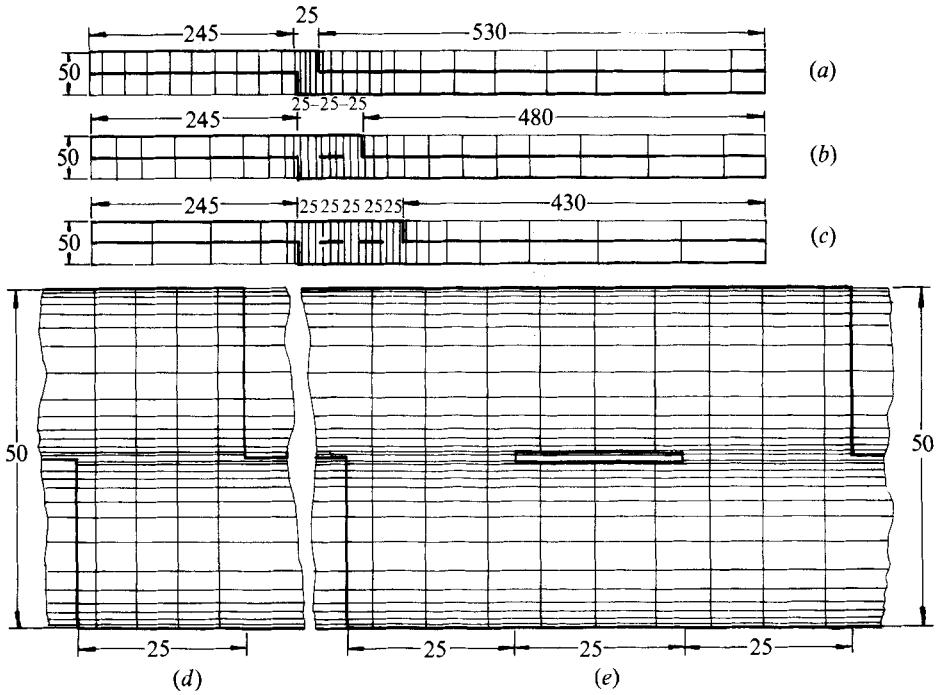

FIGURE 11. Grids. ——, gridlines; ——, solid boundary. (*a*) Stations along X-axis – single-slot case ($w/h = 1$); (*b*) stations along X-axis – two-slot case; (*c*) stations along X-axis – three-slot case; (*d*) enlarged view of the region of slot and stations along Y-axis – single-slot case; (*e*) enlarged view of the region of slots and stations along Y-axis – two-slot case. Dimensions in mm.

region which includes the slot(s). At nodes lying in this region, U is put equal to half of its value at the inlet and V is taken in the downward direction with a magnitude equal to one-fourth of U at the inlet. The choice of the initial value of V is rather arbitrary, but the choice of U takes care of the conservation of mass. Density and viscosity are constant in the present computations.

3.2.2. *Grid*

For the purpose of computation, the length of the upper channel ahead of the slot is taken to be the same as in the experiments, i.e. 245 mm. The slot width varies between 12.5 mm and 100 mm. The length of the lower channel was chosen such that the total length from the inlet to the exit is 800 mm. The justification for the choice of this length is given in the final paragraph of §3.2.3.

Calculations for $w/h = 1$ were performed with grid sizes of 18×18, 22×22, 26×26 and 30×30. Trial runs showed that for stability of computation the spacing between vertical grid lines should be smallest in the portion occupied by the slot and then it should increase gradually as the distance from the slot increases in both the upstream and downstream directions. Typical spacing for a 30×30 grid is shown in figure 11. The horizontal grid lines are chosen such that the spacing between them is smaller near the walls. Following Cebeci & Smith (1974) the grid spacing is chosen such that it increases in geometric progression as one moves from the wall to the centre of the upper or the lower channel. Thus,

$$Y_J = \frac{1-Q^{J-1}}{1-Q^{N-1}} Y_C \quad (2 \leqslant J \leqslant N),$$

where Y_J = distance of Jth point from the wall, Y_c = distance of centre from the wall, and N = number of grid points from the wall to the centre of channel. Q was chosen as 1.39. This gave a distance of 0.5 mm between the wall and the nearest grid line when the grid size was 30×30 (see figure 11 *d*, *e*).

In the two-slot case a plate 25 mm long and 1.5 mm thick separates the two slots. The choice of grid points for this case is shown in figure 11 (*b*, *e*). It is seen that the V-nodes lie on the top and bottom surfaces of the plate and along the centreline of the plate (see enlarged view in figure 11 *e*). The U-nodes lie on the vertical edges and on lines midway between the centreline and the top and bottom edges of the plate. The grid points for the three-slot case, shown in figure 11 (*c*), are obtained in a similar way.

3.2.3. *Checks on computations*

To produce numerical stability, the proper values of the under-relaxation factors were found by trials. Pun & Spalding (1977) have suggested a value of 0.5 for this factor, but a smaller value was needed when w/h was two or more.

Convergence was taken to be achieved when the highest sum of normalized residual sources along a line was less than 0.005. This required about 80 to 100 iterations. One computation takes about 6 min of CPU time on an IBM370/155 computer. It was also found that the values of U, V and p at a monitoring point, located at the middle of the slot, were constant for about the last twenty iterations.

To check whether the results are independent of the grid size, the computations were carried out for $w/h = 1$ with 18×18, 22×22, 26×26 and 30×30 grids. The profiles of the axial velocity at a station in the middle of the slot are shown in figure 12. Significant differences are found between the profiles for 18×18 and 22×22 grids. The differences between profiles for 22×22 and 26×26 grids are small and those between 26×26 and 30×30 are not noticeable. Hence a 30×30 grid was used in subsequent computations.

If the length of the computational domain is not sufficient, then the calculations would not be independent of it. Based on experience of Balachandran (1985) it was found that a length of about fourteen channel heights behind the slot was sufficient to obtain results that are independent of this length. This requires a total length, from entry to exit, of 720 mm. Hence a total length of 800 mm was chosen for all cases. It was found, after the computations, that the static pressure was constant over the entire cross-section for the last three stations along X-axis. This confirms that the chosen length of the channel was sufficient.

3.3. *Results and discussion*

3.3.1. *Single-slot case*

The computations were carried out for $w/h = 0.5$ to 4 at Reynolds number between 300 and 2000 which is the range covered in the flow-visualization studies. Computations were also done at $Re = 175$ for $w/h = 0.5$.

The computer output gives the values of U, V and p at various points in the flow field. From the velocity distributions, streamline patterns have been obtained which give the shape and extent of the regions of recirculating flow. The variation of pressure loss with w/h and Re can also be found from the computed results.

The streamline patterns for $w/h = 0.5$, 1.0 and 3.5 at selected Reynolds numbers are shown in figures 13–15. The quantity ψ in these figures is the stream function.

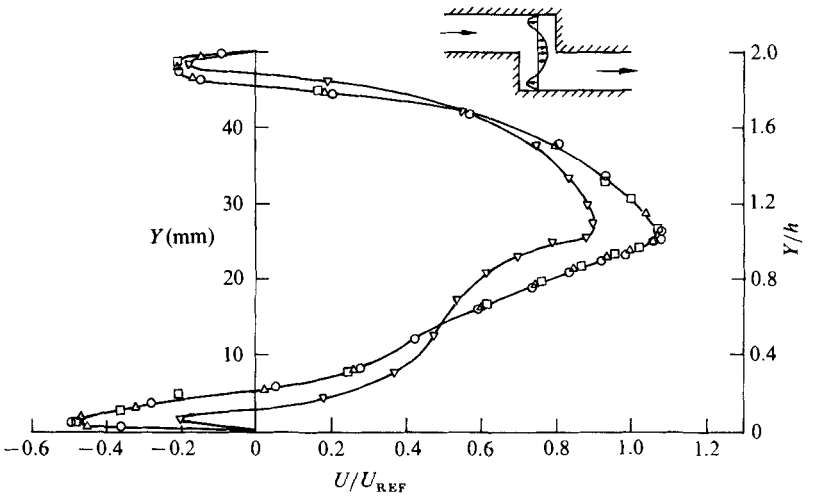

FIGURE 12. Grid-independence test: profile of U-velocity component in the middle of the slot. Symbols denote grid size: ▽, 18 × 18; □, 22 × 22; △, 26 × 26; ○, 30 × 30.

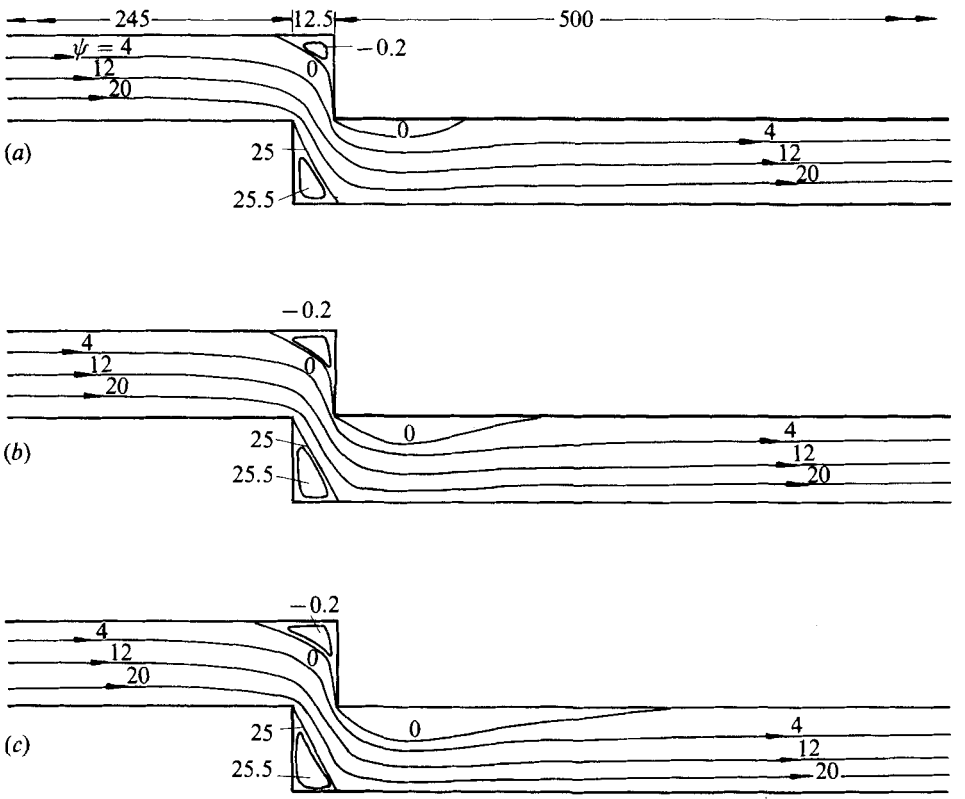

FIGURE 13. Computed flow pattern ($w/h = 0.5$). (*a*) $Re = 175$, (*b*) 600, (*c*) 2000.

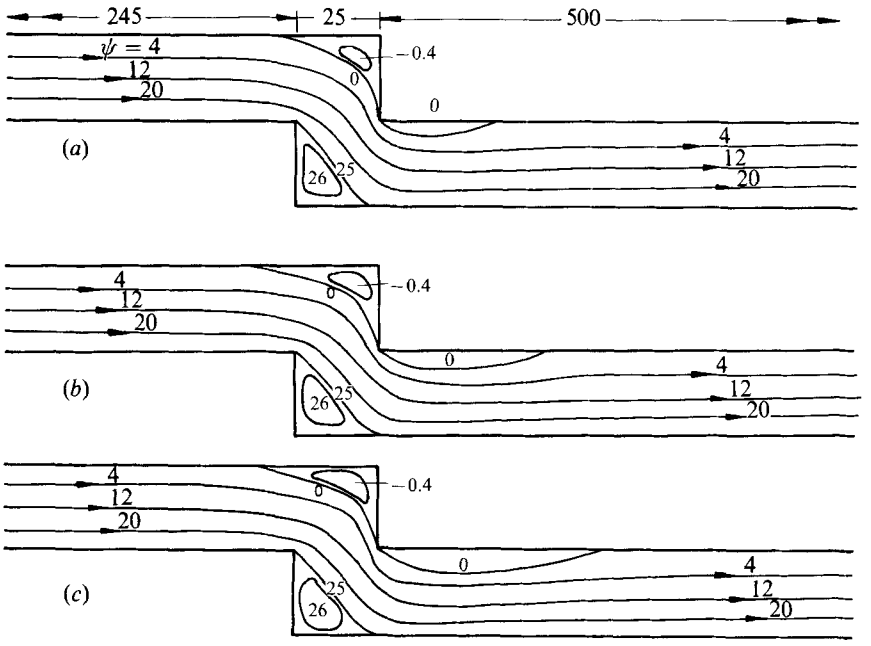

FIGURE 14. Computed flow pattern ($w/h = 1.0$). (*a*) $Re = 300$, (*b*) 600, (*c*) 2000.

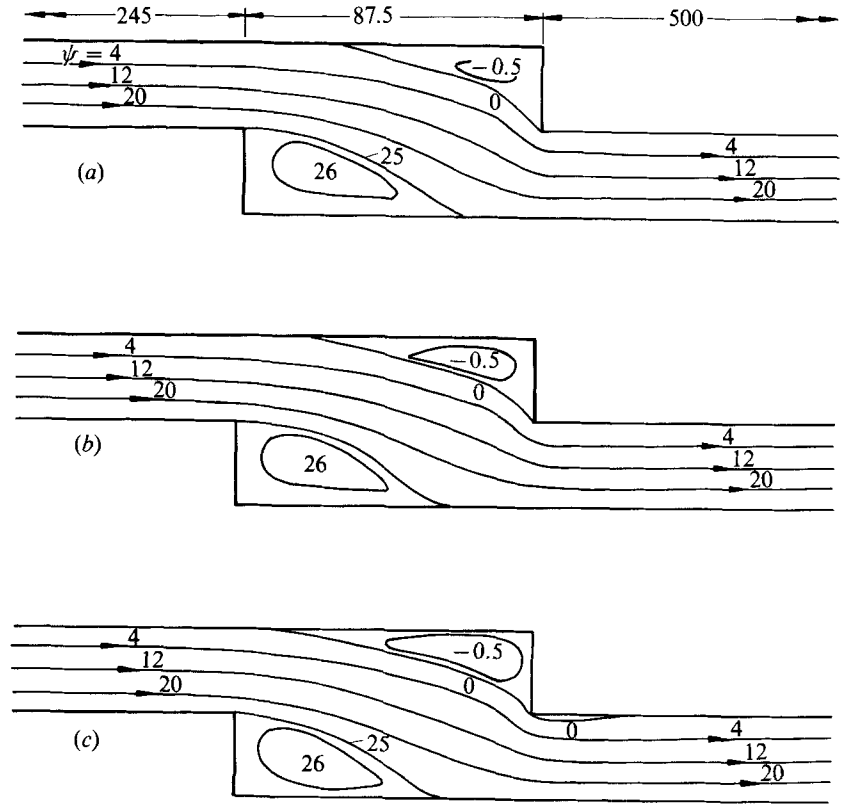

FIGURE 15. Computed flow pattern ($w/h = 3.5$). (*a*) $Re = 300$, (*b*) 600, (*c*) 2000.

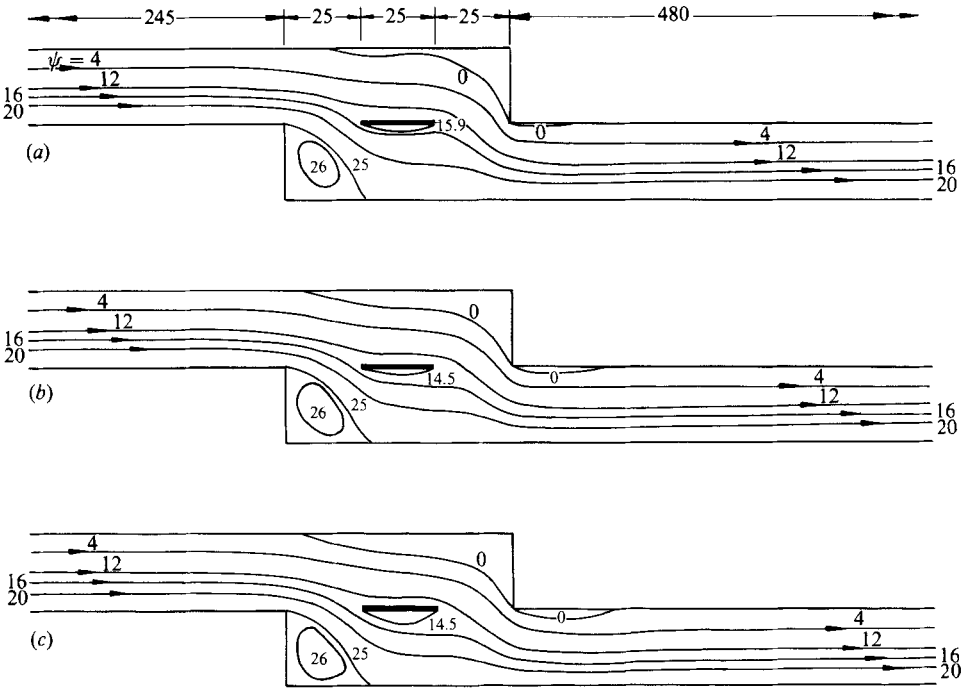

FIGURE 16. Computed flow pattern – two-slot case. (*a*) Re = 250, (*b*) 600, (*c*) 2000.

The value of ψ is zero on the top wall and is chosen as 25 on the bottom wall. The variations of the lengths L_1, L_2 and L_3 of the recirculating regions obtained from computed flow patterns are shown by solid lines in figures 6 and 7. It is seen that the length L_1 decreases as w/h increases; at low Reynolds numbers L_1 is zero for w/h greater than three (figure 7*a*, *b*). The lengths L_2 and L_3 increase with w/h. As regards the influence of Reynolds number (figure 6), the length L_1 increases gradually; L_2 remains practically constant but L_3 shows a slight increase.

Defining the pressure loss coefficient C_{PL} as

$$C_{PL} = \frac{p_i - p_e}{\frac{1}{2}\rho U_i^2},$$

where p_i and p_e are the static pressures across the inlet and exit stations respectively, ρ is the density and U_i is the velocity at the inlet, the computations show that C_{PL} decreases with Reynolds number. For example at $w/h = 1.0$, the values of C_{PL} are 6.1, 4.76, 4.28, 4.04 and 3.9 at Re = 300, 600, 1000, 1500 and 2000 respectively. At a given Reynolds number C_{PL} decreases with w/h. For example at $Re = 600$ the values of C_{PL} are 9.68, 4.76, 3.32, 2.98 and 2.82 for w/h = 0.5, 1, 2.0, 3.0 and 4.0 respectively.

3.3.2. *Multiple-slot cases*

The streamline patterns at selected Reynolds numbers are plotted for the two- and three-slot cases in figures 16 and 17. Additional regions of recirculating flow are predicted below the plates forming the slots. The depths of these regions increase as Re increases. The changes in lengths L_1 and L_2 with Re are similar to those in the single-slot case, viz. L_1 increases with Re and L_2 remains constant. However L_3 increases considerably with Re (figures 16 and 17).

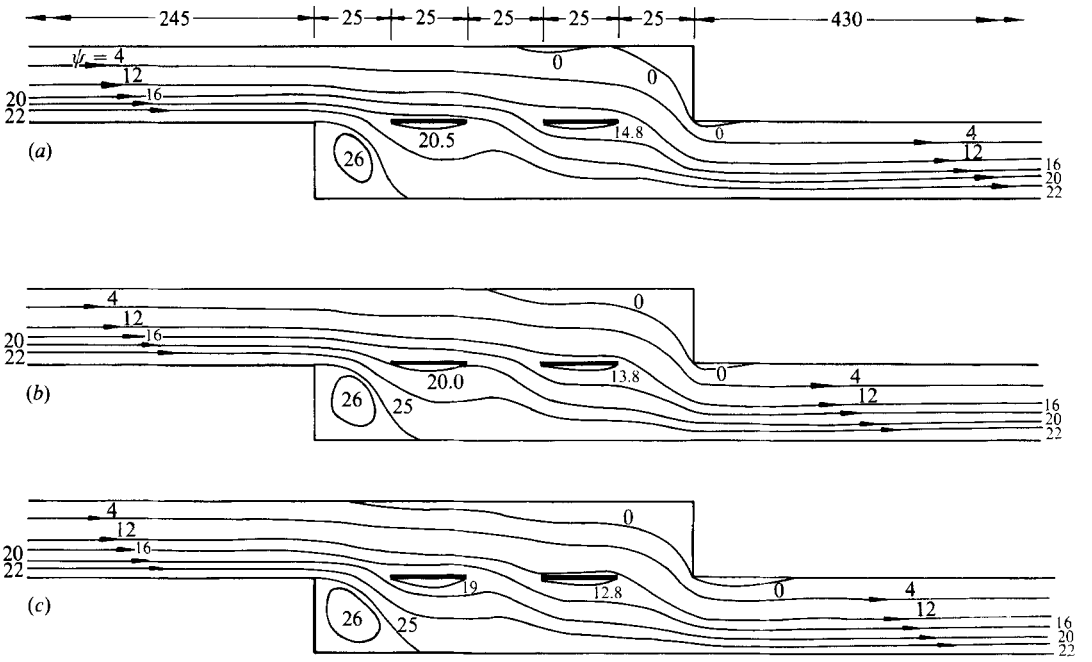

FIGURE 17. Computed flow pattern – three-slot case. (*a*) $Re = 267$, (*b*) 600, (*c*) 2000.

	Two-slot case		Three-slot case		
Re	$\dot{m}_1/\dot{m}$	$\dot{m}_2/\dot{m}$	$\dot{m}_1/\dot{m}$	$\dot{m}_2/\dot{m}$	$\dot{m}_3/\dot{m}$
300	0.364	0.636	0.18	0.228	0.592
600	0.404	0.596	0.20	0.248	0.552
2000	0.42	0.58	0.24	0.248	0.512

TABLE 1. Mass flow rates through slots

Let $\dot{m}_1$, $\dot{m}_2$, $\dot{m}_3$ be the mass flow rates through the first, second and third slot respectively and $\dot{m}$ be the total rate of mass flow through the channel. From the values of the stream functions shown in figures 16 and 17 the rates of mass flow given in table 1 can be obtained. It is seen that the fraction of mass flowing through the second slot in the two-slot case and through the third slot in the three-slot case, decreases as the Reynolds number increases. This is rather unexpected, as one would expect that with increase in *Re* a larger portion of mass flow would take place through the latter slots as velocity and consequently the inertia of the flow increases with *Re*. But the observed feature is due to the large increase in the length L_3 and the large recirculating flow near corner C_3 which restrict the available region for the fluid flow and consequently decrease the mass flow through the latter slots.

4. Comparison of experimental and computed flow patterns

A comparison of the flow patterns obtained from flow-visualization studies and those from numerical computations is presented in this section. Considering first the single-slot case it is seen that at low Reynolds number, when vortex shedding is

absent, there is qualitative agreement between the flow patterns obtained in the flow-visualization study and the computed flow patterns, e.g. figures 3(*a*) and 14(*a*); 4(*a*) and 13(*a*); 5(*a*) and 15(*a*); 5(*b*) and 15(*b*). Quantitatively the lengths L_1, L_3 and L_3 obtained from the corresponding patterns are nearly equal (see figure 7*a*, *b*). As *Re* increases the vortex shedding begins. When this occurs the two flow patterns show some differences, the details of which depend on w/h. For $w/h = 1.0$, the vortex shedding begins around $Re = 600$ near corner C_1. The length of the recirculating region decreases as seen in figures 3(*c*) and 6(*a*). With further increase in *Re*, L_1 increases and approximates the computed value. The observed and computed values of L_2 are almost equal at all Reynolds numbers (figure 6*a*). Considering the case when $w/h = 3.5$, it is seen that the vortex shedding begins at around $Re = 1000$ at corner C_3. The experimental and computed patterns begin to differ in that region. However L_1, L_2 and L_3 are nearly the same in the two cases (figure 6*c*). For $w/h = 0.5$, L_1 is nearly the same for both theory and experiment over the *Re* range covered (figure 6*b*). However, the theory gives $L_2 = 0.5h$ whereas the photographs show that $L_2 \approx h$ at all Reynolds numbers.

Comparing figures 8 and 16 and figures 9 and 17 for the two- and three-slot cases, it is seen that there is an overall agreement in the general flow patterns predicted by the theory and observed in experiments. But the present theory is unable to predict the flow details in the regions below the plates. In these regions there is rolling up, formation and shedding of vortices.

The present numerical scheme considers the steady flow solution of Navier–Stokes equations. As such it cannot predict the onset of vortex shedding and its frequency. But it is very interesting to find that, except for a small range around the Reynolds number where vortex shedding begins, the computed flow patterns closely display gross features of the actual flow field. This is because in the present case the flow is confined between walls and the fact that the same mass flow has to pass through all sections of the passage imposes a severe constraint on the extent and shape of the recirculating regions. Thus for internal flows, where the depth of the recirculating region is a sizeable part of the height of the passage, one need not solve the time-dependent Navier–Stokes equations, which is costly and time consuming. This is perhaps the reason why the calculations of turbulent flow through passages (see Launder & Spalding 1974) and even around bluff bodies in ducts (see Sampath & Ganesan 1986) carried out using steady-state equations give good predictions of velocity fields and regions of recirculating flow. However, for detailed simulations of free flow past bluff bodies, one needs to solve the time-dependent Navier–Stokes equations (see Davis & Moore 1982).

It is seen that the present numerical scheme, though able to predict the gross features of the flow, is in general, not able to reproduce the finer details of the regions of the recirculating flow. This is perhaps because this numerical scheme is of first-order accuracy. Better predictions could be expected by using higher-order methods. Particularly, caution is needed while using first-order schemes to predict turbulent recirculating flows (Castro 1979).

5. Conclusions

The following conclusions can be drawn from the above investigation of laminar flow through slots using flow visualization and numerical solution of steady-flow Navier–Stokes equations.

(i) Visualization brings out several interesting features of flow through slots. The

relative width of the slot w/h and the Reynolds number considerably influence the flow field in general and the accompanying regions of recirculating flows in particular. At very low Reynolds numbers there is no vortex shedding but the shedding starts at higher Reynolds number. The value of Reynolds number at which the shedding starts and also the corner at which it starts depend on w/h. The shape of the recirculating region, near the corner where vortex shedding begins, undergoes changes due to shedding. But with further increase in Reynolds number the depth of the recirculating region remains nearly constant and the length increases gradually, tending towards a constant value as Re approaches 2000.

(ii) The numerical results obtained by solving steady-flow Navier–Stokes equations qualitatively predict the observed flow patterns and there is reasonable quantitative agreement with some of the gross features.

The authors thank Dr. T. K. Bose for helpful discussions and Mr George Denny for help during early phases of computations.

REFERENCES

BALACHANDRAN, N. 1985 Flow through channels interconnected by Slots. MS thesis, IIT, Madras.

CARETTO, L. S., GOSMAN, A. D., PATANKAR, S. V. & SPALDING, D. B. 1973 Two calculation procedures for steady, three-dimensional flows with recirculation. In *Proc. Third Intl Conf. on Numerical Methods in Fluid Mechanics* (ed. J. Ehlers, K. Hepp & H. A. Weidenmuller), Vol. II, pp. 60–68. Springer.

CASTRO, J. P. 1979 Numerical difficulties in the computation of complex turbulent flows. In *Turbulent Shear Flows–I* (ed. F. Durst, B. E. Launder, F. W. Schmidt & J. H. Whitelaw), pp. 220–236. Springer.

CEBECI, T. & SMITH, A. M. O. 1974 *Analysis of Turbulent Boundary Layers*, p. 330. Academic.

DAVIS, R. W. & MOORE, E. F. 1982 A numerical study of vortex shedding from rectangles. *J. Fluid Mech.* **116**, 475–506.

LAUNDER, B. E. & SPALDING, D. B. 1974 The numerical computation of turbulent flows. *Computer Meth. Appl. Mech. Engng* **3**, 269–289.

PATANKAR, S. V. & SPALDING, D. B. 1972 A calculation procedure for heat mass and momentum transfer in three-dimensional parabolic flows. *Intl J. Heat Mass Transfer* **15**, 1787–1806.

PUN, W. M. & SPALDING, D. B. 1977 A general programme for two-dimensional elliptic flows. Rep. HTS/76/2. Imperial College, London.

SADDOUGHI, S. G. 1982 Analysis of potential flow through slots. MS thesis, IIT, Madras.

SAMPATH, S. & GANESAN, V. 1986 Measurements of velocity and kinetic energy of turbulence in swirling flows and their numerical prediction. *Intl J. Numer. Meth. Fluids* **6**, 229–240.

TULAPURKARA, E. G., BALACHANDRAN, N., SOLANKI, K. L., RAJAN, S. C. & DAMODARAN, K. A. 1986 Flow through channels inter-connected by slot(s). *J. Aero Soc. India* **38**, 43–47.

VASELIC-MELLING, D. 1977 Three-dimensional turbulent flow past rectangular bluff bodies. PhD thesis, London University, Imperial College, London (*Rep.* HTS /77/10).